

High-resolution conversion electron spectroscopy of the ^{125}I electron-capture decay

B. P. E. Tee,¹ A. E. Stuchbery,¹ M. Vos,² J. T. H. Dowie,¹ B. Q. Lee,¹ M. Alotiby,^{2,3} I. Greguric,⁴ and T. Kibédi^{1,*}

¹*Department of Nuclear Physics, Research School of Physics, The Australian National University, Canberra, ACT, Australia*

²*Department of Electronic Materials Engineering, Research School of Physics, The Australian National University, Canberra, ACT, Australia*

³*King Abdulaziz City for Science and Technology, Riyadh, Saudi Arabia*

⁴*Australian Nuclear Science and Technology Organisation, Lucas Heights, NSW, Australia*



(Received 17 June 2019; published 16 September 2019)

The conversion electrons from the decay of the 35.5-keV excited state of ^{125}Te following the electron capture decay of ^{125}I have been investigated at high resolution using an electrostatic spectrometer. The penetration parameter $\lambda = -1.2(6)$ and mixing ratio $|\delta(E2/M1)| = 0.015(2)$ were deduced by fitting to literature values and present data. The shake probability of the conversion electrons is estimated to be 0.5, more than two times larger than the predicted value of 0.2.

DOI: [10.1103/PhysRevC.100.034313](https://doi.org/10.1103/PhysRevC.100.034313)

I. INTRODUCTION

The probability of the emission of a conversion electron is most often evaluated from the probability of γ -ray emission and the internal conversion coefficient (ICC), α . This assumes that all nuclear structure effects are contained in the γ -ray emission probability and α only depends on atomic properties. In this case, the interaction between the conversion electron and the nucleus only takes place outside the nucleus [1]. This picture is valid for most transitions; however, the atomic electron involved in the conversion process may penetrate into the nucleus and interact with the transition charges and currents in the interior of the nucleus. The corresponding dynamic penetration matrix elements are dependent on nuclear structure and not necessarily proportional to the γ -ray matrix elements (as in the case of the pointlike nucleus assumption). These finite nucleus effects may result in anomalies in the measured ICCs, i.e., deviations from theory, which assumes pointlike nuclei. The resulting conversion coefficient of (sub)shell i , α_i , can be expressed in terms of the unperturbed conversion coefficients $\alpha_0(i, ML)$, for pure magnetic multipoles [2],

$$\alpha_i = \alpha_0(i, ML)[1 + b_1(i)\lambda + b_2(i)\lambda^2], \quad (1)$$

and $\alpha_0(i, EL)$, for pure electric multipoles [2],

$$\alpha_i = \alpha_0(i, EL)[1 + a_1(i)\eta + a_2(i)\eta^2 + a_3(i)\eta\zeta + a_4(i)\zeta + a_5(i)\zeta^2], \quad (2)$$

where $b_1(i)$, $b_2(i)$, $a_1(i)$, $a_2(i)$, $a_3(i)$, $a_4(i)$, and $a_5(i)$ are theoretical penetration coefficients of subshell i , which depend only on the electron wave functions, and λ , η , and ζ are the penetration parameters containing nuclear structure information independent of the atomic shell. For magnetic

dipole transitions, the dimensionless penetration parameter is defined to be [1,3]

$$\lambda \equiv \frac{\langle f || M_e || i \rangle}{\langle f || U_\gamma(M1) || i \rangle} \approx \frac{1}{1 + \sigma_C} \frac{\langle f || M_{e1} || i \rangle + \sigma_C \langle f || M_{e2} || i \rangle}{\langle f || U_\gamma(M1) || i \rangle}, \quad (3)$$

where $\langle f || M_{e1} || i \rangle$ and $\langle f || M_{e2} || i \rangle$ are the penetration matrix elements, $\langle f || U_\gamma(M1) || i \rangle$ is the usual $M1$ γ -radiation matrix element and σ_C is an expansion coefficient that is generally small (with magnitude between 0.1–0.2). The σ_C values are given in Ref. [4].

In a particle-core coupling model, the operators are formulated as follows [3]:

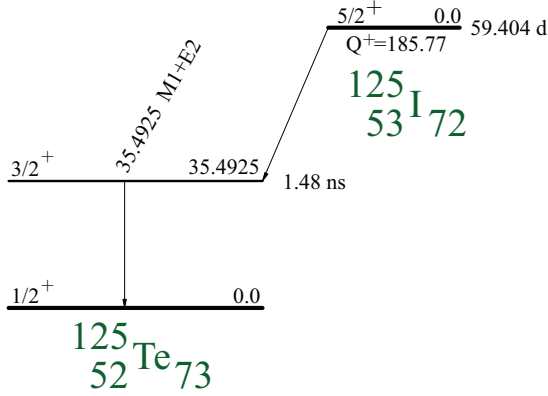
$$M_{e1} = A \left(g_l \mathbf{l} + \frac{5}{3} g_s^{(a)} \mathbf{s} + g_R \mathbf{R} + \frac{2}{3} \sqrt{2\pi} g_s^{(b)} [Y_2 \otimes \mathbf{s}]^{(1)} \right) \left(\frac{r}{R_0} \right)^2$$

$$M_{e2} = A \left(g_l \mathbf{l} + \frac{7}{3} g_s^{(a)} \mathbf{s} + g_R \mathbf{R} + \frac{4}{3} \sqrt{2\pi} g_s^{(b)} [Y_2 \otimes \mathbf{s}]^{(1)} \right) \left(\frac{r}{R_0} \right)^4$$

$$U_\gamma(M1) = A (g_l \mathbf{l} + g_s^{(M1)} \mathbf{s} + g_R \mathbf{R}), \quad (4)$$

where $A = \left(\frac{3}{4\pi}\right)^{1/2} \frac{e\hbar}{2Mc}$, \mathbf{l} and \mathbf{s} are the orbital and spin angular momentum operators for the odd nucleon and \mathbf{R} is the angular momentum operator of the core. For l -forbidden transitions the tensor term $[Y_2 \otimes \mathbf{s}]^{(1)}$ dominates. In this term (r/R_0) represents the reduced radial co-ordinate, where R_0 is the nuclear radius taken as $1.2A^{1/3}$ fm. The gyromagnetic ratios g_l , g_s , $g_R \approx Z/A$ are associated with the orbital, spin, and collective motions, respectively. Note the effective g_s factors:

*tibor.kibedi@anu.edu.au

FIG. 1. The decay scheme of ^{125}I .

$g_s^{(a)}$, $g_s^{(b)}$, and $g_s^{(M1)}$ are expected to be of the order of the free nucleon g_s value but could be different in general, and M_{e1} and M_{e2} are distinctly different from $U_\gamma(M1)$ by the appearance of the tensor term $[Y_2 \otimes s]^{(1)}$ and the overall radial integral factor. In this paper for brevity we will write the matrix elements $\langle f || Q || i \rangle$ as Q , where $Q = U_\gamma$, M_{e1} , or M_{e2} . The decay of the 35.5-keV excited state of ^{125}Te following the electron capture (EC) decay of ^{125}I is one of the few cases where the nuclear structure effect could affect the ICCs.

The decay scheme of ^{125}I into the ^{125}Te is shown in Fig. 1. The $5/2^+$ ground state of ^{125}I decays with an allowed EC transition to the 35.5-keV $3/2^+$ excited state in the ^{125}Te daughter nucleus. The direct EC decay to the $1/2^+$ ground state of ^{125}Te with a second forbidden $\Delta J = 2$ transition is highly retarded; its probability is less than 1% of the total decay intensity [5]. To EC decay to the second excited state in ^{125}Te at 144.775 keV and $J^\pi = 11/2^-$ would require a third forbidden transition with $\Delta J = 3$; it is very unlikely and not observed.

The 35.5-keV $3/2^+$ excited state decays electromagnetically to the $1/2^+$ ground state of ^{125}Te through a γ transition or the emission of a conversion electron. The selection rule for γ transitions and previous studies indicate that the 35.5-keV transition is a mixed $M1 + E2$ transition, dominantly of $M1$ multipolarity [6]. The conversion coefficient for a mixed $M1 + E2$ transition is related to $\alpha(ML)$ and $\alpha(EL)$ by

$$\alpha(M1/E2) = \frac{\alpha(M1) + \delta^2 \alpha(E2)}{1 + \delta^2}, \quad (5)$$

where the square of the multipole mixing ratio δ^2 is the ratio of the $E2$ and $M1$ γ -transition rates. The sign of δ follows the convention by Krane and Steffen [7] and δ is given by:

$$\delta = 0.835 E_\gamma \frac{\langle f || E2 || i \rangle}{\langle f || M1 || i \rangle}, \quad (6)$$

where E_γ is the transition energy in MeV, and $\langle f || E2 || i \rangle$ and $\langle f || M1 || i \rangle$ are the reduced matrix elements of the $E2$ and $M1$ operators. The $M1$ γ transition in ^{125}Te is l forbidden because the change in orbital angular momentum of the two states involved is $\Delta l = 2$ ($\nu_{d_{3/2}} \rightarrow \nu_{s_{1/2}}$). Thus the γ -ray matrix element $U_\gamma(M1)$ is expected to be small while the penetration matrix elements M_{e1} and M_{e2} are allowed due to the tensor

terms. Hence the small $U_\gamma(M1)$ with finite M_{e1} and M_{e2} may result in non-negligible λ values, causing anomalies in the observed ICCs. This scenario was first suggested by Church and Weneser [1] in 1960.

The study of anomalous ICCs resulting from the penetration effect provides an opportunity to test nuclear structure models by comparing the calculated penetration parameter λ with experiment. In the theoretical calculations of the penetration matrix elements, M_{e1} and M_{e2} are approximately proportional to the spin gyromagnetic ratio $g_s^{(b)}$ for the l -forbidden $M1$ γ transitions. The measurements of λ could therefore be used to deduce the $g_s^{(b)}$ factor, which is expected to differ from the g_s factor for free nucleons [where $g_s^{\text{free}}(p) = 5.58$ for proton, and $g_s^{\text{free}}(n) = -3.83$ for neutron] and may also differ from $g_s^{(M1)}$, which affects $M1$ transition rates and magnetic moments. Hence the renormalization of the $g_s^{(b)}$ factors can be observed in the anomalous ICC measurements and, in turn, this gives information on the spin-force constants [8,9].

^{125}I is a commonly used medical isotope. Measuring low-energy electron spectra at high precision has been part of our program to improve the knowledge of atomic radiations, including Auger electrons, for medical isotopes [10,11]. The measurements determine an accurate absolute Auger electron yield from a radioisotope by the simultaneous measurement of conversion and Auger electrons. Precise knowledge on the conversion electrons is thus required. Here we report on a measurement of the intensity ratios of conversion electrons from the l -forbidden 35.5-keV transition in ^{125}Te .

II. EXPERIMENTS

Submonolayer films of radioactive ^{125}I atoms were deposited on a Au(111) surface following the procedure described by Pronschinske *et al.* [12]. The ^{125}I activity was obtained commercially from PerkinElmer (part number: NEZ033A002MC) and the sources were prepared at the Australia's Nuclear Science and Technology Organisation (ANSTO). The Au(111) surface was obtained by flame annealing the Au samples just before the ^{125}I deposition. A droplet containing Na ^{125}I in a 100 μL 0.02 M NaOH solution ($\text{pH} \approx 10$) was put on this surface, and left to react. An approximately 4 mm diameter source with an activity of 5 MBq was obtained in this way.

The conversion electron measurements were performed using an electrostatic spectrometer that is capable of measuring electrons with energies from 2 keV up to 40 keV [13,14]. A layout of the electrostatic spectrometer is presented in Fig. 2 along with a simulation of the electron transport through the spectrometer. The sample was held at the center of a positive high-voltage hemisphere in an ultrahigh vacuum ($\approx 10^{-10}$ mbar) chamber. At the exit of the hemisphere, the emitted electrons are collimated by passing through a 0.5 mm wide slit before entering into a decelerating lens system (close to ground potential) followed by a hemispherical analyzer. The lens system decelerates the electrons to the pass energy and focuses them at the entrance of the analyzer. The electrons are then detected by a two-dimensional detector after passing through a hemispherical analyzer, and the precise energy is calculated from the impact position. SIMION simulations [15]

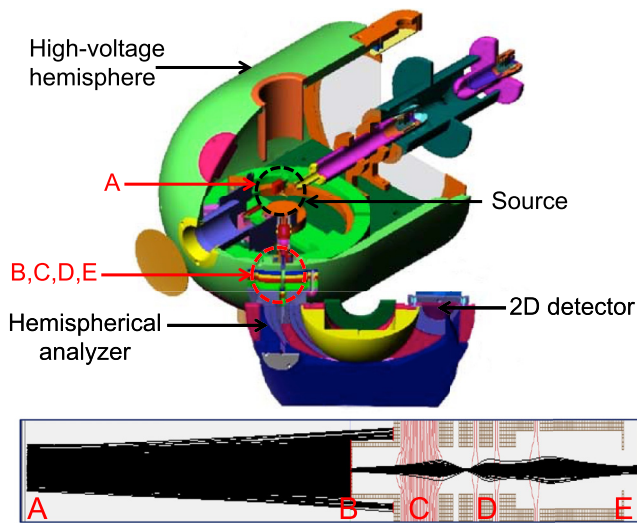


FIG. 2. Top: Layout of the electrostatic spectrometer [13,14]. The details are described in the main text. Bottom: SIMION simulations for the electrostatic spectrometer. Electrons emitted from a 4 mm diameter source (A) are restricted from entering the lens stack by a 0.5 mm wide slit (B). After the main deceleration stage (C) the electrons are focused by a set of electrostatic lenses (D) on the exit plane (E) that coincides with the entrance of the hemispherical analyzer. The vertical scale is expanded by a factor of 4 for clarity, and the red lines are equipotential planes plotted at 1000 V intervals.

show that all electrons transmitted through the slit will enter the analyzer (see the bottom panel in Fig. 2), hence the spectrometer transmission is determined solely by the width of the entrance slit and is independent of the electron kinetic energy. This spectrometer was operated in two different modes: A high-resolution mode and a low-resolution mode.

In the high-resolution mode the pass energy was set to 200 eV. The sample high-voltage was kept constant and the analyzer voltage was varied up to 1 kV. Stability of the sample

high voltage was checked using a precision voltage divider and a seven-digit volt meter, and found to be better than 0.2 V. However the absolute accuracy of the high-voltage measurement is not expected to be better than 5 V. The energy resolution was found to be 4.8 eV in this mode but the range of energies that can be measured was limited to ≈ 930 eV due to constraints on the voltage that can be applied to the analyzer.

In the low-resolution mode the pass energy was set to 1000 eV, the analyzer voltage was kept constant and the sample high voltage was controlled by a computer using a 16-bit DAC. Measurement of the obtained voltage in this mode showed deviations up to 8 V from the nominal voltage when the high voltage was varied between 5 kV and 35 kV, but when the voltage is varied over a smaller range (1–2 kV) the deviation was fairly constant (≈ 1 V) over this range. The energy resolution was found to be 6.6 eV in this mode, and the energy range that can be measured is not restricted so that the data acquisition rate is about five times higher.

Five measurements on the conversion electrons were carried out as presented in Figs. 3 and 4. Figure 3 shows the spectrum of the L conversion electrons measured in two different modes: The L_1 , L_2 , and L_3 conversion electrons measured together in the low-resolution mode, and the L_1 conversion electron measured in the high-resolution mode. Figure 4 shows the spectrum of the L_1 , $M_{1,2,3}$, and N_1 conversion electrons measured in the low-resolution mode and in three groups: Fig. 4(a) L_1 , M_1 , and M_2 , 4(b) M_1 , M_2 , and M_3 , and 4(c) M_1 and N_1 .

III. SPECTRUM EVALUATION

All measured conversion peaks are observed to be asymmetric with a longer tail on the low-energy side. The tails generally can be attributed to energy loss of (inelastically scattered) electrons, due to intrinsic and extrinsic effects. Intrinsic effects involve a sudden change in the atomic potential due to formation of a core hole causing an outer-shell

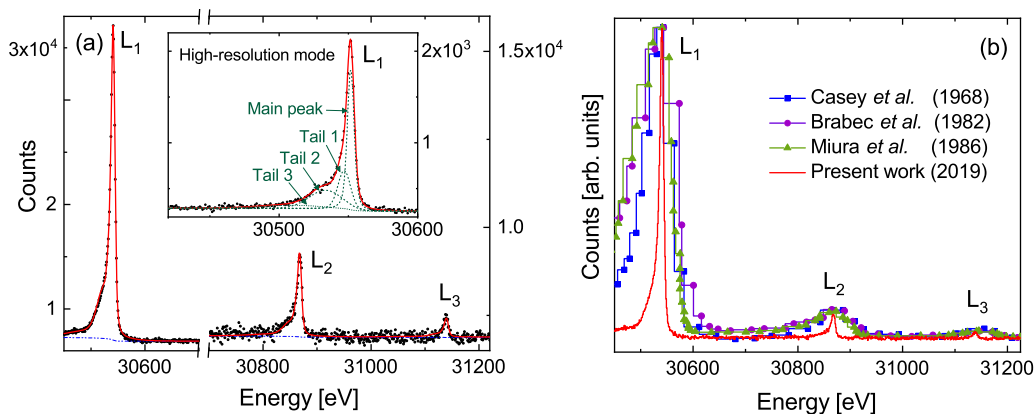


FIG. 3. (a) The L_1 , L_2 , and L_3 conversion lines spectrum taken at 6.6 eV instrumental resolution, with natural widths of 2.2 eV, 2.84 eV, and 2.62 eV, respectively, as adopted from Campbell *et al.* [16]. The fitted curve and the background are shown in red and blue dashed curves, respectively. Note that the L_2 and L_3 lines are on a different scale to the L_1 line. The reduced χ^2 of this fit is 1.9. The L_1 peak measured at high resolution of 4.8 eV is shown in the insert to illustrate the fitting procedure. (b) Comparison of the L_1 , L_2 , and L_3 conversion electrons of present measurements (low-resolution mode) with those taken using magnetic spectrometers by Miura *et al.* [17], Brabec *et al.* [18], and Casey *et al.* [19]. All previous data were digitized and scaled to match the L_1 peak height of the present data.

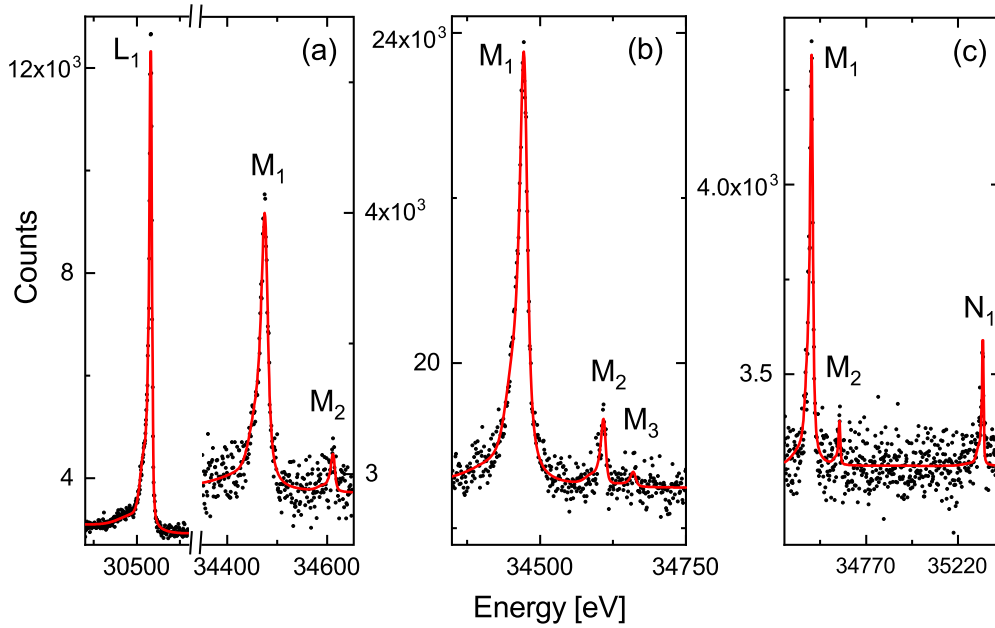


FIG. 4. Spectra from three separate measurements in low-resolution mode: (a) L_1 conversion line measured together with M_1 and M_2 . A 3 keV region between the peaks is omitted. (b) M_1 , M_2 and M_3 conversion lines. (c) M_1 , M_2 , and N_1 conversion lines. The adopted natural widths of 10.2 eV, 3.2 eV, 3.9 eV, and 2.4 eV for the M_1 , M_2 , M_3 , and N_1 lines were taken from Campbell *et al.* [16].

electron to be excited into another bound state or into the continuum, i.e., the shake processes [20,21]. Extrinsic effects involve the transportation of electrons through the solid from the emitting atom to the surface, causing inelastic scattering leading to creation of surface plasmons. Given the sample was a monolayer source, the contribution of bulk plasmons is expected to be small, and the probability of surface plasmon creation at these high energies (30–35 keV) is of order of 3% [15]. Thus it is expected that the observed tails are mostly due to the shake processes, that is, the intrinsic effects.

The fitting strategy is as follows: Individual conversion electron peaks were fitted by convoluting a Lorentzian function with the sum of four Gaussian functions. The Lorentzian component is used to describe the lifetime broadening effects of a core shell, and the Gaussian components describe the instrumental broadening effects. Additional broadening was included in each tail component, attributed to the shake processes, by introducing a free-fitting parameter to indicate the intrinsic width of a tail in its Gaussian profile. The Gaussian widths of the tails are therefore a combination of both intrinsic tail widths, t_w , and instrumental resolution, w_G , with a magnitude of $\sqrt{t_w^2 + w_G^2}$. The Lorentzian (natural) widths of conversion lines were adopted from the latest compilation of recommended natural widths data by Campbell *et al.* [16]. In addition, a very small Shirley-type background [22] was implemented in the fit to account for the small increment in the observed background under the peaks. A fit showing the components of a fitted line is illustrated in Fig. 3(a).

To determine the peak area of different conversion electron lines with as few free parameters as possible, it was assumed that all conversion electrons have the same tail distributions. This assumption was based on the following reasons: (i) The shake probabilities of the conversion electrons measured

here were calculated and found to be similar [23], using the methodology proposed by Krause and Carlson [24]. (ii) There is no reliable theory at present to describe the energy distribution of the shake electrons. In order to study the line shapes of the conversion electrons, the most intense (L_1) conversion line was measured in the high-resolution mode. From this measurement, a set of tail parameters was obtained, as summarized in Table I. This set of tail parameters was then employed for all other conversion lines, by adjusting, for a given conversion peak, the Gaussian and Lorentzian widths to account for the different spectrometer resolutions and the lifetimes of the core shells.

The energies of the conversion electrons can be calculated by adopting the electron binding energies from the literature [25]. In an actual experiment, there are several factors that can result in deviations of the measured energies from the predicted values. These factors include whether the energies were measured relative to the Fermi level, the effect of chemical shifts, which depend on the chemical environment of the radioactive source, and differences due to the use of different voltage supplies in high- and low-energy resolution modes. Indeed, these effects shift all core level energies in the same way, and the energy separations between the conversion peaks generally agree very well with the literature values. Therefore

TABLE I. Adopted tail parameters in the fitting of all conversion lines.

Parameter	Tail No. 1	Tail No. 2	Tail No. 3
Shift to the main peak (eV)	5	18	42
Intensity relative to main peak	0.4	0.5	0.2
Intrinsic width (eV)	8	24	55

they were kept fixed during the fitting processes at the values from Ref. [25].

Various fits were made to the conversion electron spectra by taking natural widths from Campbell *et al.* [16], Krause and Oliver [26], Fuggle and Alvarado *et al.* [27], or from the EADL database [28]. The effect of employing different fitting approaches on the measured quantities was assessed and included in the quoted uncertainties.

IV. RESULTS

The results from the current conversion electron measurements are summarized in Table III, which also lists the literature and theoretical values. Note that the calculated ICCs are given for two different sets of the nuclear parameters (the λ penetration parameter and the $\delta(E2/M1)$ mixing ratio). One set is from the previous work of Brabec *et al.* [18], and one from the present analysis (see Sec. V below).

The $L_1:L_2:L_3$ intensity ratios from the present measurement are $1 : 0.085(3) : 0.019(3)$. These are consistent with the ratios reported by Geiger *et al.* [29] and Coursol *et al.* [30]. The obtained $L_1:L_2$ ratio appears to be larger, but consistent with, the ratios reported by Brabec *et al.* [18] and Casey *et al.* [19], where both studies used magnetic spectrometers. In comparison, the present measurement has a higher-energy resolution, which is illustrated in the right panel of Fig. 3. All measured $L_1:L_3$ ratios are similar, except for the ratio obtained by Casey *et al.* [19], which we consider as an outlier. Note that Casey *et al.* [19] quoted a 20% uncertainty on their $L_1:L_2$ ratio but a 5% error in their $L_1:L_3$ ratio, which does not seem correct, as the L_2 line is much more intense than the L_3 line. The $L_1:M_1$ intensity ratio was found to be $1 : 0.202(5)$, which is in agreement with the predicted ratio of $1 : 0.198$. The L_1 to M_1 intensity ratio is not sensitive to the change in mixing ratio $\delta(E2/M1)$ and penetration parameter λ (see Table III). Considering the energy difference between L_1 and M_1 conversion lines, the fact that the measured ratio is in agreement with the theoretical expectations indicates that the transmission of the electrostatic spectrometer was indeed not sensitive to the energy, which is in accord with SIMION simulations. The measured $L_1:M_2$ intensity ratio is $1 : 0.017(3)$. However, this ratio was not included in the analysis, as from the $L_1:M_1$ ratio and $M_1:M_2:M_3$ ratios a more accurate $L_1:M_2$ ratio can be deduced. The $M_1:M_2:M_3$ intensity ratios are $1 : 0.095(6) : 0.023(7)$. The $M_1:M_2$ ratio agrees broadly with the ratios reported by Coursol *et al.* [30] and Brabec *et al.* [18]. The $M_1:M_3$ intensity ratio is close to the ratio reported by Brabec *et al.* [18], but is much larger than the value reported by Coursol *et al.* [30]. Finally, the M_1 conversion peak was measured together with the N_1 conversion peak. This measurement also revealed the M_2 conversion peak, however, this peak was too weak to obtain accurate information on its intensity. Note that the M_3 conversion peak could not be observed in this case due to its low yield. The intensity ratio of M_1 and N_1 conversion lines measured here is $1 : 0.18(2)$, which is slightly larger than the ratio reported by Brabec *et al.* [18]. Nevertheless, both measured ratios are consistent with the predicted value of $1 : 0.198$, which is insensitive to the change in nuclear parameters, λ and δ .

TABLE II. Theoretical internal conversion coefficients for pure $M1$ and $E2$ transitions (calculated using BRICC [25]) and the b_1 and b_2 penetration coefficients (calculated using a modified version of the code CATAR [32]) for the 35.5-keV transition in ^{125}Te .

Orbital shell	$\alpha_0(M1)$	$\alpha_0(E2)$	b_1	b_2
K	$1.17E+1$	$1.31E+1$	$-1.31E-2$	$4.32E-5$
L_1	$1.41E+0$	$1.34E+0$	$-1.36E-2$	$4.61E-5$
L_2	$1.13E-1$	$2.06E+1$	$-2.04E-3$	$1.06E-6$
L_3	$2.83E-2$	$2.93E+1$	$-1.37E-5$	$8.49E-10$
M_1	$2.80E-1$	$2.75E-1$	$-1.36E-2$	$4.65E-5$
M_2	$2.37E-2$	$4.28E+0$	$-2.14E-3$	$1.16E-6$
M_3	$5.91E-3$	$6.18E+0$	$-1.46E-5$	$9.51E-10$
M_4	$2.65E-4$	$5.41E-2$	$-3.13E-6$	$8.26E-10$
M_5	$1.89E-4$	$6.46E-2$	$<1E-10$	$<1E-10$
N_1	$5.58E-2$	$5.50E-2$	$-1.36E-2$	$4.66E-5$
N_2	$4.39E-3$	$7.89E-1$	$-2.16E-3$	$1.18E-6$
N_3	$1.08E-3$	$1.14E+0$	$-1.47E-5$	$9.72E-10$
N_4	$4.14E-5$	$8.36E-3$	$-3.20E-6$	$8.43E-10$
N_5	$2.92E-5$	$9.91E-3$	$<1E-10$	$<1E-10$
O_1	$6.19E-3$	$6.10E-3$	$-1.36E-2$	$4.66E-5$
O_2	$3.42E-4$	$6.15E-2$	$-2.16E-3$	$1.19E-6$
O_3	$8.13E-5$	$8.49E-2$	$-1.47E-5$	$9.74E-10$

V. DISCUSSION

A. Internal conversion coefficients and the nuclear parameters

The multipolarity of the 35.5-keV transition from the decay of the $3/2^+$ excited state of ^{125}Te is known to be almost pure ($>99\%$) $M1$. Therefore the impact of the penetration effect is considered only for the magnetic transition. The conversion coefficients of (sub)shell i are then related to λ and $\delta(E2/M1)$, as given by Eq. (1) and Eq. (5):

$$\alpha_{i,\text{exp}} = \frac{\alpha_0(i, M1)[1 + b_1(i)\lambda + b_2(i)\lambda^2] + \delta^2\alpha_0(i, E2)}{1 + \delta^2}. \quad (7)$$

Note the theoretical penetration coefficients $b_1(i)$ and $b_2(i)$ are constants for a given atomic shell. The conversion coefficients for pure magnetic dipole and electric quadrupole transitions of (sub)shell i [$\alpha_0(i, M1)$ and $\alpha_0(i, E2)$, respectively] are adopted from the BRICC code [25], and $b_1(i)$ and $b_2(i)$ were calculated using Dirac Hartree-Fock-Slater wave functions [31] in a modified version of the code CATAR [32]. The adopted values of $\alpha_0(i, M1)$, $\alpha_0(i, E2)$, $b_1(i)$, and $b_2(i)$ are shown in Table II. A similar expression can also be obtained for the ratios of i and j subshell conversion coefficients:

$$\left(\frac{\alpha_i}{\alpha_j}\right)_{\text{exp}} = \frac{\alpha_0(i, M1)[1 + b_1(i)\lambda + b_2(i)\lambda^2] + \delta^2\alpha_0(i, E2)}{\alpha_0(j, M1)[1 + b_1(j)\lambda + b_2(j)\lambda^2] + \delta^2\alpha_0(j, E2)}. \quad (8)$$

The optimum values of λ and δ can be extracted from the experimental data using a least-squares fitting method. The associated χ^2 value is given by

$$\chi^2 = \sum_{k=1}^n \frac{[O_k - T(R_k, \lambda, \Delta)]^2}{\sigma_k^2}, \quad (9)$$

where O_k , σ_k , and $T(R_k, \lambda, \Delta)$ are the experimental quantities and the corresponding uncertainties and theoretical values, of measurement k , respectively. The evaluation of the least-squares fitting was done by using MINUIT with the MIGRAD minimizer, and the standard errors were obtained from the MINUIT processor MINOS [33]. Using Eq. (7), Eq. (8), and Eq. (9), and the current and previous experimental values from Table III, the best-fit values of $\lambda = -1.2(6)$ and $|\delta| = 0.015(2)$ were obtained, with a reduced $\chi^2 = 1.2$. Some literature values were excluded in the least-squares approach, since they are more than two standard deviations away from the corresponding fitted values (see Table III and Fig. 5). The ratios of the experimental values to the calculated values with this set of nuclear parameters is shown in Fig. 5. The figure also compares the current evaluated values with the previously evaluated values determined by Brabec *et al.* [18]. The $\lambda = -1.2(6)$ value obtained in the present analysis indicates a smaller anomaly in the conversion coefficients than reported previously. In order to compare this value with theory, we have calculated λ using the intermediate coupling approach in the particle-vibrational (PV) model, in which an odd neutron is coupled to the quadrupole vibrations of a spherical core, and the coupling strength is described by a dimensionless parameter ξ . The formulations can be found in Ref. [3,45,46]. In the calculations, the $2s_{1/2}$, $1d_{3/2}$, $1d_{5/2}$, and $0g_{7/2}$ shell-model orbits were considered and the extra-core nucleon was coupled to one and two phonon core excitations. Radial integrals over the reduced coordinate (r/R_0) were evaluated with harmonic oscillator wave functions with phase chosen so that the wave functions are positive as $r \rightarrow \infty$. This phase convention is implicit in the formulation of the PV model Hamiltonian in that the coupling parameter ξ is positive for all single-particle orbits. The renormalization of the $g_s^{(b)}$ factor was chosen to be 0.6 according to the results in Ref. [8], and it was assumed that $g_s^{(a)} = g_s^{(M1)} = g_s^{(b)}$. This assumption is reasonable for the hindered $M1$ transitions since the terms associated with the $g_s^{(a)}$ and $g_s^{(M1)}$ factors in Eq. (4) are small relative to the term associated with $g_s^{(b)}$. The following g factors: $g_s^{(b)} = 0.6 \times g_s^{\text{free}}$, $g_l = 0.0$, $g_R = 0.4$ were used and the coupling strength parameter was taken to be $\xi = 3.0$, which is reasonable and near maximal for nuclei in this mass region [46]. The calculation results are summarized and compared in Table IV. The calculated g factors of the $1/2^+$ and $3/2^+$ states are close to their experimental values, and the calculated $E2$ transition strength between these two states is also consistent with the experimental value. This agreement indicates that the PV model describes the dominant part of the $1/2^+$ and $3/2^+$ state wave functions reasonably well. As a consequence of the small $M1$ strength, the magnitude of the calculated $\lambda = +5.6$ is about five times larger than the experimental value, and the predicted sign is not in accord with our analysis. The overestimation of λ stems from the underestimation of $U_\gamma(M1)$ [or equivalently the $B(M1)$] as indicated in Table IV. Thus the PV basis is clearly not sufficient to describe $U_\gamma(M1)$ accurately. The main contribution to the calculated $U_\gamma(M1)$ comes from the configuration mixing of higher states into the transition states. Also, additional currents due to meson exchange and/or velocity dependent forces, which are usually small for allowed transitions [1], are not being considered in

TABLE III. Mixing ratios, penetration parameters and internal conversion coefficients for the 35.5-keV transition in ^{125}Te . The experimental values are compared with the previous and present evaluated sets of nuclear parameters.

Quantity	Exp.	Ref.	Calculated	
			$\lambda = +2.4^a$ $ \delta = 0.029$	$\lambda = -1.2^b$ $ \delta = 0.015$
$100/(1 + \alpha_{\text{Tot}})$	6.68(14) 6.55(13)	1990Iw04 [34] 1992ScZZ [35]	7.01	6.73
α_{Tot}	13.65(28) 14.25(64)	1969Ka08 [36] 1979CoZG [30]	13.26	13.86
$\alpha_K/(1 + \alpha_{\text{Tot}})$	0.80(5) 0.804(10)	1952Bo16 [37] 1970Ma51 [38]	0.795	0.800
$\alpha_L/(1 + \alpha_{\text{Tot}})$	0.11(2)	1952Bo16 [37]	0.109	0.107
$\alpha_M/(1 + \alpha_{\text{Tot}})$	0.020(4)	1952Bo16 [37]	0.022	0.021
K	12.01(18) 11.90(31)	1969Ka08 [36] 1979CoZG [30]	11.33	11.88
L	1.4(1)	1999Sa55 [39]	1.55	1.59
K/L	12.3(25)	1969Ca01 [19]	7.30	7.47
L/M	5.21(26)	1982Br16 [18]	5.00	5.00
M/N	4.87(20)	1982Br16 [18]	5.08	5.07
L_2/L_1	0.089(4) 0.106(21) 0.082(4) 0.095(2) ^c 0.085(3)	1965Ge04 [29] 1969Ca01 [19] 1979CoZG [30] 1982Br16 [18] Present	0.095	0.082
L_3/L_1	0.024(2) 0.041(2) ^c 0.019(3) 0.023(5) 0.019(3)	1965Ge04 [29] 1969Ca01 [19] 1979CoZG [30] 1982Br16 [18] Present	0.039	0.025
M_1/L_1	0.202(5)	Present	0.198	0.198
M_2/M_1	0.092(5) 0.101(5) ^c 0.095(6)	1979CoZG [30] 1982Br16 [18] Present	0.101	0.087
M_3/M_1	0.044(3) ^c 0.030(5) 0.023(7)	1979CoZG [30] 1982Br16 [18] Present	0.042	0.026
N_1/M_1	0.214(6) ^c 0.18(2)	1982Br16 [18] Present	0.199	0.199
δ^d	+0.09(1) ^c +0.095(25) ^c +0.078(12) ^c +0.08(3) ^c +0.04(8) +0.12(7) -0.002(16) -0.02(13) +0.04(6)	1971Ba44 [41] 1971Ba44 [41] 1971Ba44 [41] 1971Wy02 [42] 1971Wy02 [42] 1971Wy02 [42] 1972Ba12 [43] 1972Ba12 [43] 1972Ba12 [43]	0.029	0.015

^aPreviously evaluated values by Brabec *et al.* [18].

^bEvaluated values from the present analysis.

^cExcluded in the present least-square fitting analysis.

^dThe quoted experimental values from the angular distribution and correlation measurements are from the compilation by Krane [40].

the formulated $U_\gamma(M1)$ operator in Eq. (4). Such small currents could possibly explain the observed discrepancy. Since the penetration matrix elements M_{e1} and M_{e2} are not sensitive to the choice of parameters (except the g_s factor), a common

TABLE V. Comparison of the penetration parameter λ for the $M1 + E2$ transition ($\nu_{d_{3/2}} \rightarrow \nu_{s_{1/2}}$) for the $^{121,123,125}\text{Te}$ isotopes.

Nucleus	γ energy (keV)	$ \delta(E2/M1) $	Measured λ	Calculated $ \lambda $			
				Ref. [8] ^a	Ref. [48] ^a	Ref. [49]	PV model ^b
^{121}Te	212.2	0.226(8) [51]	−0.7(17) [52] −3 to +4 [53]	1.0	1.1	0.6–0.8	0.6
^{123}Te	159.0	0.062(6) [54]	−2(2) [55]	1.2	1.3	0.6–0.8	0.8
^{125}Te	35.5	0.015(2)	−1.2(6)	1.2	1.4	0.7–0.8	0.8

^aEvaluated with effective g factor $g_s^{\text{eff}} = 0.6 \times g_s^{\text{free}}$.

^bParticle-vibration model. Present calculations.

of deducing the sign of λ in ^{125}Te , the signs of λ in ^{121}Te and ^{123}Te are deduced to be negative. Thus our results suggest the core-polarization theory does not describe the l -forbidden $\nu_{d_{3/2}} \rightarrow \nu_{s_{1/2}}$ transitions in the Te isotopes correctly. More precise measurements on the ^{121}Te and ^{123}Te isotopes could help to draw a firm conclusion on this problem.

The evaluated mixing ratio of $|\delta| = 0.015(2)$ is in accord with $|\delta| = 0.019$, predicted by [43], using the Kisslinger-Sørensen model. The sign of this quantity cannot be deduced from ICC measurements because of the quadratic dependence on δ in Eq. (5).

B. Shake processes

The observed tails on the conversion lines are expected to be due to the shake processes. Our high-resolution measurements provide an opportunity to study the shake electrons emitted from outer shells. Assuming that the tails correspond to shake electrons, using Table I, the shake probability for Te can be estimated from the fitted tail intensities: $100\% \times (0.4 + 0.5 + 0.2)/(1 + 0.4 + 0.5 + 0.2) \approx 50\%$ of the total peak area. This value is more than two times larger than the predicted value of $\approx 20\%$, obtained from a calculation based on the single-configuration framework [23]. It should be noted that this model does not take into account the electron-electron correlations. There are at least two possible explanations for the discrepancy between expected and observed shake intensity: (i) the large overlap between the tail and the main peak may have overestimated the tail intensity, and/or (ii) the shake probability calculations based on the single-configuration framework may underestimate the effect. Calculations that exclude the electron-electron correlations are mainly valid for closed-shell atoms. Lowe *et al.* [56] demonstrated that the inclusion of electron-electron correlations in the calculations of shake probability describe better the transition metals (which all have an open $3d$ shell). Their calculated probabilities are up to seven times larger than the ones based on the single-configuration framework. Tellurium has six valence electrons and atomic configuration of $5s_{1/2}^2 5p_{1/2}^2 5p_{3/2}^2$, i.e., it has an open $5p$ shell, which might likewise signal the importance of correlations and help explain the observed high shake probability.

The energy distribution of the shake electrons associated with a transition of energy E_γ can be described using the following equation [24]:

$$E_{\text{shake}} + E_{\text{core}} = E_\gamma - E_i - E_j^*, \quad (11)$$

where $E_\gamma = 35.5$ keV, E_{shake} and E_{core} are the kinetic energies of the shake and core electrons, respectively. E_i is the binding energy of (sub)shell i (where the core electron is emitted), and E_j^* is the binding energy of (sub)shell j (where the shake electron is emitted) with a vacancy present in (sub)shell i . Note that E_j^* is approximately the binding energy of (sub)shell j , and in this case the core electron is the conversion electron. The emitted conversion electron and shake electron are indistinguishable, hence the result is a continuous energy distribution from zero energy up to $E_\gamma - E_i - E_j^*$. Since the shake electrons are mostly from the N_4 , N_5 , O_1 , O_2 , and O_3 subshells [23], which have binding energies of 40.8 eV, 39.2 eV, 11.6 eV, 2.6 eV, and 2.0 eV, respectively [25], the tail shift parameters in Table I are of the correct magnitude to correspond to these binding energies. Differences between the fit energies and the outer-shell binding energies may be influenced by the use of a symmetrical (Gaussian) peak shape in the fit, whereas the actual energy distribution of the shake electrons is expected to be asymmetric [57]. Further investigations are needed to make a more quantitative evaluation of the shake processes.

VI. CONCLUSION

High-resolution electron spectroscopy following the electron-capture decay of ^{125}I has been reported. By combining the present and literature values of conversion electron intensity ratios, we have evaluated new values of the penetration parameter, $\lambda = -1.2(6)$, and the $E2/M1$ mixing ratio, $|\delta| = 0.015(2)$, for the 35.5-keV ($\nu_{d_{3/2}} \rightarrow \nu_{s_{1/2}}$) transition in ^{125}Te . The magnitude of λ is consistent with our calculated $|\lambda| = 0.8$ using the particle vibrational (PV) model with the experimental $U_\gamma(M1)$, and is also consistent with other theoretical values using alternative nuclear models [8,48,49]. The negative sign of λ is not consistent with the theoretical prediction of Ref. [49], which adopts a core-polarization approach, whereas it agrees with our semiempirical analysis based on the sign of the mixing ratio [6] and the calculated sign of the $E2$ γ matrix element. Nonetheless, since λ is small, the penetration effect on the internal conversion coefficients is less than 4% for this case. The obtained $|\delta|$ is in agreement with the theoretical prediction in Ref. [43].

The electron shake processes arising from the emission of the conversion electrons has also been investigated. It was found that the measured shake probability for the L , M , and N conversion electrons is about 50%, which is 2.5 times larger

than the predicted value of 20%, based on single-configuration calculations [23]. Our results may indicate the importance of the inclusion of electron-electron correlations in the shake-probability calculations for an open shell atom such as Te.

As noted in Sec. I, a primary aim of the present measurements was to determine the Auger electron yields for the medical isotope ^{125}I by simultaneously measuring the Auger electron yields relative to the conversion electron yields. The present paper has focused on the nuclear parameters λ and δ , which affect the conversion electron yields of the relevant l -forbidden 35.5 keV nuclear $M1$ transition in ^{125}Te . The Auger electron yields have been published elsewhere [10,11] and compared with results of computational models [58,59]. These recently published Auger yields were based on conversion electron yields evaluated with the nuclear parameters determined here.

Looking to future experimental evaluations of Auger yields from radioisotopes by this method, it appears that penetration

effects are generally small for spherical nuclei in this mass region [8,49]. However, much larger penetration factors have been reported in some cases [60]. Because the measurement of penetration factors is so difficult, it is important to have a reliable estimate on whether they are significant or not. The present theoretical analysis suggests that for l -forbidden $M1$ transitions, a useful estimate of the magnitude can be obtained by combining a theoretical model for the allowed electron penetration matrix elements with the experimental forbidden $M1$ γ -radiation matrix element.

ACKNOWLEDGMENTS

This research was made possible by an Australian Research Council Discovery Grant DP140103317. J.T.H.D. acknowledges support of the Australian Government Research Training Program.

-
- [1] E. Church and J. Weneser, *Annu. Rev. Nucl. Sci.* **10**, 193 (1960).
 [2] H.-C. Pauli, *Helv. Phys. Acta* **40**, 713 (1967).
 [3] G. V. Berghe and K. Heyde, *Nucl. Phys. A* **144**, 558 (1970).
 [4] E. L. Church, Tech. Rep. BNL-50002 (Brookhaven National Lab., Upton, 1966).
 [5] K. M. Smith and G. M. Lewis, *Nucl. Phys.* **89**, 561 (1966).
 [6] J. Katakura, *Nucl. Data Sheets* **112**, 495 (2011).
 [7] K. S. Krane and R. M. Steffen, *Phys. Rev. C* **2**, 724 (1970).
 [8] M. A. Listengarten, V. M. Mikhailov, and A. P. Feresin, *Izv. Akad. Nauk SSSR, Ser. Fiz.* **40**, 712 (1976).
 [9] M. A. Listengarten, *Izv. Akad. Nauk SSSR, Ser. Fiz.* **42**, 1823 (1978).
 [10] M. Alotiby, I. Greguric, T. Kibédi, B. Q. Lee, M. Roberts, A. E. Stuchbery, P. Tee, T. Tornyi, and M. Vos, *Phys. Med. Biol.* **63**, 06NT04 (2018).
 [11] M. Alotiby, I. Greguric, T. Kibédi, B. Tee, and M. Vos, *J. Electron. Spectrosc. Relat. Phenom.* **232**, 73 (2019).
 [12] A. Pronschinske, P. Pedevilla, C. J. Murphy, E. A. Lewis, F. R. Lucci, G. Brown, G. Pappas, A. Michaelides, and E. C. H. Sykes, *Nature Mater.* **14**, 904 (2015).
 [13] M. Vos, G. P. Cornish, and E. Weigold, *Rev. Sci. Instrum.* **71**, 3831 (2000).
 [14] M. R. Went and M. Vos, *J. Electron. Spectrosc. Relat. Phenom.* **148**, 107 (2005).
 [15] D. A. Dahl, *Int. J. Mass Spectrom.* **200**, 3 (2000).
 [16] J. L. Campbell and T. Papp, *At. Data Nucl. Data Tables* **77**, 1 (2001).
 [17] T. Miura, Y. Hatsukawa, M. Yanaga, K. Endo, H. Nakahara, M. Fujioka, E. Tanaka, and A. Hashizume, *Hyperfine Interact.* **30**, 371 (1986).
 [18] V. Brabec, M. Ryšavý, O. Dragoun, M. Fišer, A. Kovalik, C. Ujhelyi, and D. Berényi, *Z. Phys. A* **306**, 347 (1982).
 [19] W. R. Casey and R. G. Albridge, *Z. Phys. A* **219**, 216 (1969).
 [20] T. A. Carlson and C. W. Nestor, *Phys. Rev. A* **8**, 2887 (1973).
 [21] S. K. Srivastava and A. Bahadur, *Leonardo J. Sci.* **8**, 50 (2009).
 [22] D. A. Shirley, *Phys. Rev. B* **5**, 4709 (1972).
 [23] B. Q. Lee, Ph.D. thesis, Australian National University, 2017, <https://doi.org/10.25911/5d6fa12d942aa>.
 [24] M. O. Krause and T. A. Carlson, *Phys. Rev.* **158**, 18 (1967).
 [25] T. Kibédi, T. Burrows, M. Trzhaskovskaya, P. M. Davidson, and C. Nestor Jr., *Nucl. Instrum. Methods Phys. Res., Sect. A* **589**, 202 (2008).
 [26] M. O. Krause and J. Oliver, *J. Phys. Chem. Ref. Data* **8**, 329 (1979).
 [27] J. C. Fuggle and S. F. Alvarado, *Phys. Rev. A* **22**, 1615 (1980).
 [28] S. T. Perkins, D. E. Cullen, M.-H. Chen, J. H. Hubbell, J. Rathkopf, and J. H. Scofield, Lawrence Livermore National Laboratory Report UCRL-50400, 30 (1991).
 [29] J. S. Geiger, R. L. Graham, I. Bergstrom, and F. Brown, *Nucl. Phys.* **68**, 352 (1965).
 [30] N. F. Coursol, Ph.D. thesis, CEA Saclay, 1980.
 [31] D. Liberman, D. Cromer, and J. Waber, *Comput. Phys. Commun.* **2**, 107 (1971).
 [32] H. C. Pauli and U. Raff, *Comput. Phys. Commun.* **9**, 392 (1975).
 [33] F. James, *MINUIT: Function Minimization and Error Analysis: Reference Manual Version 94.1*, CERN-D506 (1994).
 [34] A. Iwahara, M. H. H. Marechal, C. J. Da Silva, and R. Poledna, *Nucl. Instrum. Methods Phys. Res. A* **286**, 370 (1990).
 [35] U. Schötzgig, H. Schrader, and K. Debertin, in *Nuclear Data for Science and Technology* (Springer, Berlin, 1992), pp. 562–564.
 [36] E. Karttunen, H. U. Freund, and R. W. Fink, *Nucl. Phys. A* **131**, 343 (1969).
 [37] J. C. Bowe and P. Axel, *Phys. Rev.* **85**, 858 (1952).
 [38] A. Märelius, K. G. Vålivaara, Z. Awwad, J. Lindskog, J. Phil, and S.-E. Håggglund, *Phys. Scr.* **1**, 91 (1970).
 [39] M. S. Sarkar, *Phys. Rev. C* **60**, 064309 (1999).
 [40] K. S. Krane, *At. Data Nucl. Data Tables* **19**, 363 (1977).
 [41] J. Barrette, M. Barrette, A. Boutard, G. Lamoureux, and S. Monaro, *Nucl. Phys. A* **169**, 101 (1971).
 [42] L. D. Wyly, J. B. Salzberg, E. T. Patronis, N. S. Kendrick, and C. H. Braden, *Phys. Rev. C* **3**, 2442 (1971).
 [43] T. Badica, S. Dima, A. Gelberg, and I. Popescu, *Z. Phys. A* **249**, 321 (1972).
 [44] R. S. Narcisi, Tech. Rep. 2-9 (Harvard University Press, Cambridge, 1959).
 [45] D. C. Choudhury and T. F. O'dwyer, *Nucl. Phys. A* **93**, 300 (1967).

- [46] K. Heyde and P. J. Brussaard, *Nucl. Phys. A* **104**, 81 (1967).
- [47] S. K. Chamoli, A. E. Stuchbery, and M. C. East, *Phys. Rev. C* **80**, 054301 (2009).
- [48] I. V. Kopytin and M. A. Dolgoplov, *Izv. Akad. Nauk SSSR, Ser. Fiz.* **42**, 2445 (1978).
- [49] B. S. Rao, *Phys. Lett. B* **56**, 435 (1975).
- [50] A. Giannatiempo, A. Perego, and A. Passeri, *Z. Phys. A* **319**, 153 (1984).
- [51] S. Ohya, *Nucl. Data Sheets* **111**, 1619 (2010).
- [52] L. O. Edvardson, L. Westerberg, G. C. Madueme, and L. Samuelsson, *Phys. Scr.* **4**, 45 (1971).
- [53] H. S. Sahota, *Indian J. Phys.* **47**, 729 (1973).
- [54] S. Ohya, *Nucl. Data Sheets* **102**, 547 (2004).
- [55] S. Törnkvist, S. Ström, and L. Hasselgren, *Nucl. Phys. A* **130**, 604 (1969).
- [56] J. A. Lowe, C. T. Chantler, and I. P. Grant, *Phys. Rev. A* **83**, 060501(R) (2011).
- [57] T. Mukoyama, *X-Ray Spectrom.* **34**, 64 (2005).
- [58] B. Q. Lee, H. Nikjoo, J. Ekman, P. Jönsson, A. E. Stuchbery, and T. Kibédi, *Int. J. Radiat. Biol.* **92**, 641 (2016).
- [59] M. H. Chen, B. Crasemann, and H. Mark, *Phys. Rev. A* **21**, 442 (1980).
- [60] T. R. Gerholm, B. G. Pettersson, and Z. Grabowski, *Nucl. Phys.* **65**, 441 (1965).